An improved land biosphere module for use in reduced complexity Earth System Models with application to the last glacial termination

Roland Eichinger[1], Gary Shaffer[2,3], Nelson Albarrán[4], Maisa Rojas[1], and Fabrice Lambert[5]

[1]Department of Geophysics, University of Chile, Blanco Encalada 2002, Santiago, Chile
[2]GAIA-Antarctica, University of Magellanes, Avenida Bulnes 01855, Punta Arenas, Chile
[3]Niels Bohr Institute, University of Copenhagen, Blegdamsvej 17, Copenhagen, Denmark
[4]Department of Physics, University of Santiago de Chile, Avenida Ecuador 3493, Santiago, Chile
[5]Department of Physical Geography, Catholic University of Chile, Vicuña Mackenna 4860, Santiago, Chile

Correspondence to: Roland Eichinger (roland@dgf.uchile.cl)

Abstract.

   Interactions between the land biosphere and the atmosphere play an important role for the Earth's carbon cycle and thus should be considered in studies of global carbon cycling and climate. Simple approaches are a useful first step in this direction but may not be applicable for certain climatic conditions. To improve the ability of the reduced-complexity Danish Center

5 for Earth System Science (DCESS) Earth System Model DCESS to address cold climate conditions, we reformulated the model's land biosphere module by extending it to include three dynamically varying vegetation zones as well as a permafrost component. The vegetation zones are formulated by emulating the behavior of a complex land biosphere model. We show that with the new module, the size and timing of carbon exchanges between atmosphere and land are represented more realistically in cooling and warming experiments. In particular, we use the new module to address carbon cycling and climate change across

10 the last glacial transition. Within the constraints provided by various proxy data records, we tune the DCESS model to a Last Glacial Maximum state and then conduct transient sensitivity experiments across the transition under the application of explicit transition functions for high latitude ocean exchange, atmospheric dust, and the land ice sheet extent. We compare simulated time evolutions of global mean temperature, pCO$_2$, atmospheric and oceanic carbon isotopes as well as ocean dissolved oxygen concentrations with proxy data records. In this way we estimate the importance of different processes across the transition with

15 emphasis on the role of land biosphere variations.

1 Introduction

On centennial to millennial time scales, ocean processes may largely determine variations of atmospheric CO$_2$ concentrations (Fischer et al., 2010; Sigman et al., 2010). Such processes include changes in ocean dynamics as well as in biogeochemical properties like variations in the phosphate inventory or iron fertilisation (Martin et al., 1990; Maher et al., 2010). However,

20 also interactions between atmosphere and land can have an important impact on the overall change in the carbon cycle and thus on the Earth's climate system. Net primary production on land takes up CO$_2$ from the atmosphere at a rate that increases with the pCO$_2$ itself (CO$_2$ fertilisation; Saugier et al., 2001). Remineralisation in the soils increases with increasing tempera-

ture (Davidson and Janssens, 2006). Different vegetation zones advance and retreat due to varying climate conditions, thereby changing the terrestrial biomass budget and thus the carbon amount being stored in vegetation (Ciais et al., 2012). Moreover, changes in permafrost area and, during glacial conditions, changes in areas covered by ice sheets also have the potential to significantly modify atmospheric pCO_2 significantly (Schuur et al., 2008). The release of carbon into the atmosphere through the thawing of permafrost in a warming future climate has been assessed in a number of studies (e.g. Schaefer et al., 2011; Schuur et al., 2008; Khvorostyanov et al., 2008) and carbon storage and release in and from permafrost can also help explain glacial-interglacial cycles (Zech, 2012; Ciais et al., 2012; Crichton et al., 2016). A land biosphere module within an Earth System Model should be able to address these processes.

For this reason, we here extend the Danish Center for Earth System Sciences (DCESS) Earth System Model (Shaffer et al., 2008) by a new terrestrial biosphere scheme. This parameterisation features the three vegetation zones, tropical forests (TF), grasslands-savanna-deserts (GSD) and extratropical forests (TF), through definition of their characteristic values of biomass reservoirs and net primary production (NPP). The dynamic accounting of the latitudinal boundaries of the different zones and thereby their area extents is approximated by fitting polynomial functions of global mean temperature (T_{glob}) to results of a complex vegetation model study by Gerber et al. (2004). For completeness we also developed a simple approach to vegetation albedo based on the relative sizes of the three vegetation zones. Moreover, we present a component that accounts for carbon being stored in permafrost and below terrestrial ice sheets to allow extensive carbon storage on land during glacial climate conditions and its release across deglaciation events. In DCESS model simulations, these new developments considerably improve the estimates of amount and timing of land-atmosphere carbon exchanges, including the carbon isotopes ^{13}C and ^{14}C.

For a first application of this new module, we furthermore developed a set of explicit functions that describe the transitions of high latitude ocean exchange, atmospheric dust and land ice sheet extent across the last 25 kaBP. This allows us to simultaneously simulate time series of global mean temperature, pCO_2, atmospheric and oceanic carbon isotopes as well as ocean dissolved oxygen concentrations across the deglaciation after the Last Glacial Maximum (LGM, ~21,000 years ago). Hitherto, the DCESS model has been used mainly for future climate projections (see e.g. Shaffer et al., 2009; Shaffer, 2010) and evaluated for pre-industrial (PI) climate conditions (see Shaffer et al., 2008). For the present application, the model is calibrated to glacial conditions by adapting physical and biogeochemical parameters guided by proxy data records. This includes a physically simple method to generate isolated deep water in the high latitude model ocean (as it had been hypothesised by several studies, e.g. Francois et al., 1997; Sigman and Boyle, 2000; Broecker and Barker, 2007) through the imposition of a depth profile for the vertical exchange intensity. Transient sensitivity simulations across the last 25 kaBP are then performed. These demonstrate the impact and timing of various processes on atmospheric temperatures, pCO_2 and the carbon isotopes ^{13}C and ^{14}C at the beginning of the last glacial termination ("Mystery Interval" (MI), from 17.5 to 14.5 kaBP; Broecker and Barker, 2007) and reveals that carbon outgassing from permafrost and uptake of carbon by the land biosphere broadly compensate each other during the temperature rise of the early last deglaciation.

2 A new land biosphere in the DCESS model

The DCESS model features components for the atmosphere, ocean, ocean sediment, land biosphere and lithosphere and has been designed for global climate change simulations on time scales from years to millions of years (Shaffer et al., 2008). Its geometry consists of one hemisphere, divided into two 360° wide zones by 52° latitude. The model ocean is divided into a low-mid and a high latitude sector (as in the HILDA (**hi**gh-**l**atitude exchange/interior **d**iffusion **a**dvection) model, developed by Shaffer and Sarmiento, 1995) and features a continuous vertical resolution of 100 m, to a depth of 5500 m. The near surface atmospheric mean temperature is described by a simple, zonal mean, energy balance model in combination with sea ice and snow parameterisations. The atmosphere is assumed to be well mixed for gases and air-sea gas exchange fluxes and transports via weathering, volcanism and interactions with the land biosphere are considered for carbon dioxide (CO_2) and methane (CH_4) in $^{12,13,14}C$ species, respectively, as well as for nitrous oxide (N_2O) and oxygen (O_2). Ocean dynamics are characterised by high latitude sinking and low-mid latitude upwelling as well as horizontal and vertical diffusion between the latitude zones and the ocean layers. For the ocean biogeochemical cycling, a number of tracers are considered (namely, phosphate (PO_4), dissolved oxygen (O_2), dissolved inorganic carbon ($DI^{12,13,14}C$), and alkalinity (ALK)), which are forced by new production, air-sea exchange, remineralisation of organic matter, dissolution of $CaCO_3$, river inputs and evaporation/precipitation (Shaffer, 1996; Shaffer et al., 2008). There is a sediment section for each of the ocean model layers addressing $CaCO_3$ dissolution/burial and organic matter remineralisation/burial.

A land biosphere scheme accounts for the $^{12,13,14}C$ cycling with leaf, wood, litter and soil boxes (Shaffer et al., 2008). NPP on land takes up CO_2 from the atmosphere and is distributed between leaves and wood. Leaf loss goes to litter, wood loss is divided between litter and soil and litter loss is divided between the atmosphere (as CO_2) and the soil. Soil loss goes to the atmosphere as CO_2 and CH_4. Losses from all land reservoirs are taken to be proportional to reservoir size and, for litter and soil, to depend upon the mean atmospheric temperature according to $\lambda_Q \equiv Q_{10}^{(T_{glob}-T_{glob,PI})/10}$, where Q_{10} (a biotic activity increase for a 10 degree increase of T_{glob}) is chosen to be 2 (Friedlingstein et al., 2006). With this simplified vegetation scheme, the DCESS model responds to cooling with an increase in land biomass. The terrestrial remineralisation rate decreases with sinking temperatures and hence, more carbon can be stored below ground. However, LGM reconstructions show less carbon in the land biosphere than for warmer, pre-industrial conditions (Peng et al., 1998; Prentice et al., 2011). This simplistic model behaviour can be seen in Fig. 1a, which shows the steady state terrestrial biomass as a function of pCO_2 and T_{glob}. These results are generated through prescribing various pCO_2 and T_{glob} values in numerous 2 ka model simulations.

In an attempt to remedy these deficiencies while retaining simplicity on the level of the rest the model, we here present the extension of this scheme to three different vegetation zones. We define a latitudinal distinction of three different vegetation zones and their latitudinal boundaries on a global scale. The zones we consider are tropical forests (TF), grasslands, savanna and deserts (GSD) and extratropical forests (EF) containing temperate and boreal forests. In the new version (Fig. 1b), biomass decreases when temperatures sink as vegetation types shift and the snow line moves equatorward (note however that a pre-scribed ice sheet line is not included in these simulations). The permafrost biomass, however, increases in the course of that process. This shows that the general land carbon storage is represented more realistically in the new model version. In this
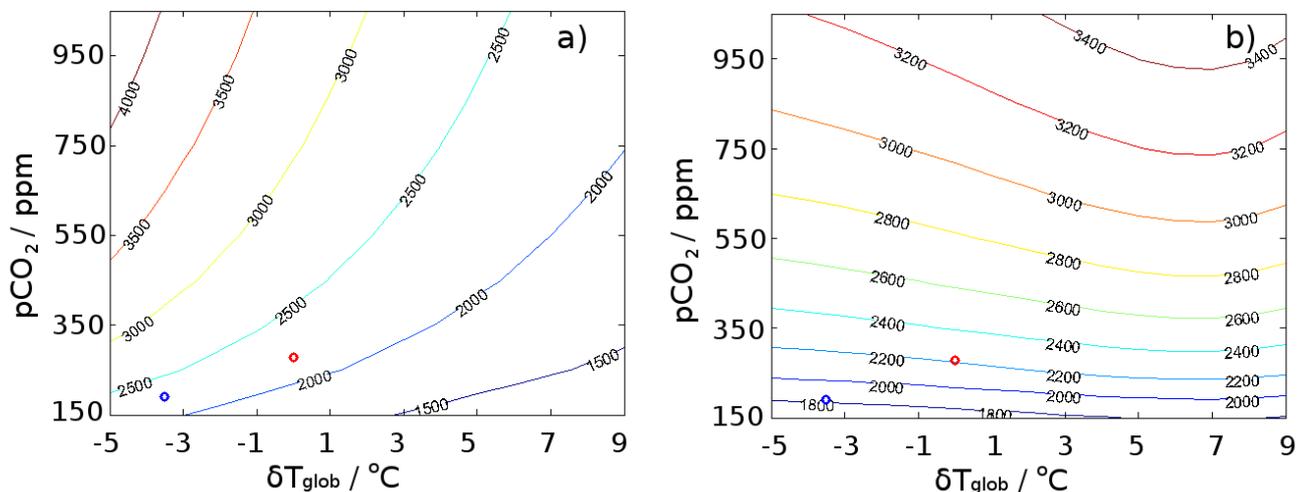
Figure 1. Steady state land biomass (GtC) as a function of global mean temperature ($^\circ$C) and pCO$_2$ (ppm) deviations from the calibrated PI value for a) the old uniform biosphere scheme and b) the new biosphere scheme with three vegetation zones. The red circles denote the PI and the blue circles LGM conditions.

section, we first present the characteristics of the chosen vegetation zones and their latitudinally variable borders. Then, the new calculations of the biosphere-atmosphere exchange fluxes of CO$_2$ and CH$_4$ for ^{12}C as well as for the rare carbon isotopes ^{13}C and ^{14}C are described and a simplified formulation of the treatment of permafrost is given. Moreover, in this section, we provide a brief evaluation of the new vegetation module, to show how it represents land-atmosphere carbon fluxes on centennial

5 to millennial time scales.

2.1 Description of the vegetation zones

The three vegetation zones (TF, GSD, BF) were defined on the basis of a study by Gerber et al. (2004). In that study, the complex LPJ terrestrial biosphere model (Lund-Potsdam-Jena Dynamic Global Vegetation Model) was applied to distinguish between a number of vegetation zones based on several variables. Tab. 1 shows the characteristic values of biomass reservoirs

10 and net primary production (NPP) of those vegetation zones at PI climate conditions for one hemisphere (Gower et al., 1999; Saugier et al., 2001; Sterner and Elser, 2002; Zheng et al., 2003; Chapin et al., 2011). The values in Tab. 1 have been constrained such that the sum over the three vegetation zones adds up to PI values of the original biosphere model (Shaffer et al., 2008).

The latitudinal limits of these vegetation zones are dynamically defined. In general, the extent of certain vegetation zones depends mainly on temperatures and precipitation. However, the limitations of the DCESS model (no explicit computation of precipitation and restriction to two latitudinal sections) require a somewhat more general approach. We therefore determine the division of the three vegetation zones solely by the deviation of the global mean atmosphere temperature from its PI value. For this purpose, we derived two polynomial functions from a study by Gerber et al. (2004, in particular from the results in their

	Tropical forest	Grassland savanna desert	Boreal forest
Leaves / GtC	15	10	25
Wood / GtC	135	90	25
Litter / GtC	8	32	20
Soil / GtC	100	400	250
NPP / $Gt \cdot a^{-1}$	12.5	7.5	10

Table 1. Distribution of biomass reservoirs and net primary production of the different vegetation zones at PI conditions, globally averaged for one hemisphere adjusted to the DCESS model geometry (see Chapin et al., 2011, and citations therein).

Fig. 4). This emulation of a complex vegetation model thereby implicitly includes the role of precipitation in the temperature-dependence of the vegetation zone boundaries. The two latitudinal limitations of the vegetation zones are described by the two 5th order polynomials

$$
\begin{aligned}
L_{TF-GSD} = & -1.83 \cdot 10^{-5} \cdot \delta T_{glob}^5 - 0.0005809 \cdot \delta T_{glob}^4 - 0.005168 \cdot \delta T_{glob}^3 \\
& + 0.0497 \cdot \delta T_{glob}^2 + 1.092 \cdot \delta T_{glob} + 11.28
\end{aligned}
\tag{1}
$$

and

$$
\begin{aligned}
L_{GSD-EF} = & \; 1.152 \cdot 10^{-5} \cdot \delta T_{glob}^5 - 0.0001785 \cdot \delta T_{glob}^4 - 0.004557 \cdot \delta T_{glob}^3 \\
& + 0.04156 \cdot \delta T_{glob}^2 + 1.017 \cdot \delta T_{glob} + 37.77,
\end{aligned}
\tag{2}
$$

which depend only on the deviation of the global mean atmosphere temperature δT_{glob} from the calibrated PI steady-state. L_{TF-GSD} denotes the latitude of the border between the TF and the GSD zones and L_{GSD-EF} the latitude between GSD and EF. These two 5th order polynomials are illustrated in Fig. 2.

The EF vegetation zone additionally is limited by either the model "snowline" (defined as the latitude of $0°C$ global mean temperature) or the line of the terrestrial ice sheet extent, depending on which one of the two lines expands the farthest from the pole at the current time step (see Sect. 2.3). The snowline is also included in Fig. 2. Based on these latitudinal limits, the total CO_2 and CH_4 fluxes between the terrestrial biosphere and the atmosphere are now determined by the sum of the three vegetation zones and thereby depend on the areas and mean temperatures of each zone as well as their values of NPP and stored biomass.

Furthermore for completeness and consistency, we extended the model albedo calculation to account for the new biosphere scheme with the three vegetation zones. Non-forest vegetation zones, in our case the GSD zone, have a higher albedo than
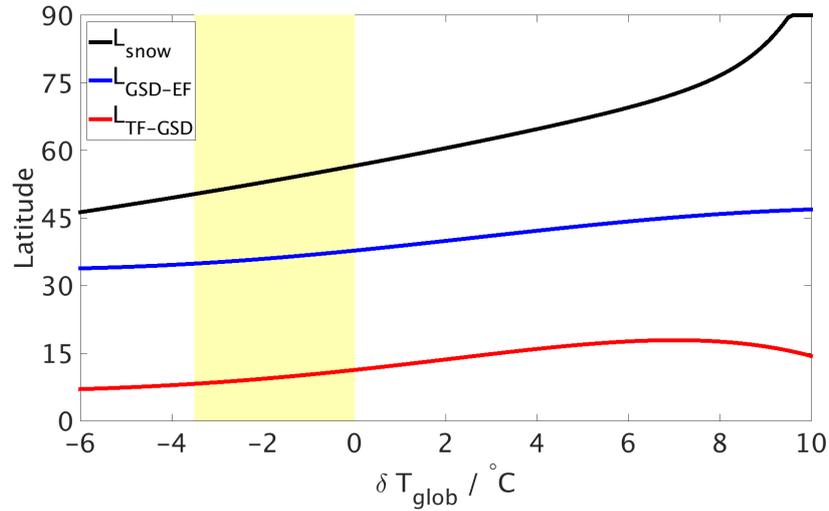
Figure 2. Polynomial functions describing the dynamic latitudes of the borders between the three vegetation zones as function of the global mean atmosphere temperature (δT_{glob}) deviation and the latitude of 0°C global mean atmosphere temperature L_{snow} (black). Red: Border between the TF and the GSD zone (L_{TF-GSD}). Blue: Border between the GSD and the EF zone (L_{GSD-EF}). The yellow bar marks the region between LGM and PI climate conditions. (PI: $\delta T_{glob,PI} = 0°C$, $L_{TF-GSD,PI} = 11.28°$, $L_{GSD-EF,PI} = 37.77°$, $L_{snow,PI} = 55°$); LGM: ($\delta T_{glob,LGM} = -3.5°C$; $L_{TF-GSD,LGM} = 7.17°$; $L_{GSD-EF,LGM} = 33.92°$, $L_{snow,LGM} = 47°$)

forest zones, here the TF and the EF zones (Bonan, 2008). Based on the latitudinal approach by Hartmann (1994) that was applied to the DCESS model (Shaffer et al., 2008), we now also take into account the ratio of the GSD vegetation zone to the overall vegetation area for the albedo calculation. For this, the model was calibrated to give a vegetation albedo radiative forcing anomaly of about -0.7 W·m^{-2} for LGM conditions. Such details are found in the supplementary material.

2.2 Extension of the carbon flux equations

In the original version of the DCESS terrestrial biosphere module (Shaffer et al., 2008), the global vegetation NPP is determined by

$$NPP = NPP_{PI}\left(1 + f_{CO2} \cdot ln\left(\frac{pCO_2}{pCO_{2,PI}}\right)\right). \tag{3}$$

10 Now, we subdivide this equation into three equations

$$NPP_{TF} = NPP_{TF,PI} \cdot A_{TF} \cdot \left(1 + f_{CO2} \cdot ln\left(\frac{pCO_2}{pCO_{2,PI}}\right)\right), \tag{4}$$

$$NPP_{GSD} = NPP_{GSD,PI} \cdot A_{GSD} \cdot \left(1 + f_{CO2} \cdot ln\left(\frac{pCO_2}{pCO_{2,PI}}\right)\right) \tag{5}$$

and

$$NPP_{EF} = NPP_{EF,PI} \cdot A_{EF} \cdot \left(1 + f_{CO2} \cdot ln\left(\frac{pCO_2}{pCO_{2,PI}} \right) \right) \tag{6}$$

for the different vegetation zones, respectively. Thus, the global NPP is now determined by the sum of the NPP of the three vegetation zones:

$$NPP = NPP_{TF} + NPP_{GSD} + NPP_{EF} \tag{7}$$

The factors A_{TF}, A_{GSD} and A_{EF} are calculated by

$$A_{TF} = \frac{sin(L_{TF-GSD})}{sin(L_{TF-GSD,PI})}, \tag{8}$$

$$A_{GSD} = \frac{sin(L_{GSD-EF} - L_{TF-GSD})}{sin(L_{GSD-EF,PI} - L_{TF-GSD,PI})} \tag{9}$$

and

$$A_{EF} = \frac{sin(L_s) - sin(L_{GSD-EF})}{sin(L_{s,PI}) - sin(L_{GSD-EF,PI})} \tag{10}$$

and scale the contributions of the respective NPP by the current area of the individual vegetation zone. The index PI stands for reference PI conditions and f_{CO2} for the CO$_2$ fertilisation factor. In the original configuration, this factor was set to 0.65, which was in good agreement with results by Friedlingstein et al. (2006). However, a revision of this value in a model intercomparison study yielded a lower value of 0.37 to be a more suitable value for the terrestrial biosphere (Zickfeld et al., 2013) and thus has also been used in the present study. Analogously, the land biosphere methane production (LBMP) (see Shaffer et al., 2008) is now calculated separately for the three vegetation zones as well.

Now, the four conservation equations per carbon isotope (^{12,13,14}C) (see Shaffer et al., 2008) have to be calculated for each vegetation zone separately. The losses for reservoir size of litter and soil were dependent on the mean global atmosphere temperature in Shaffer et al. (2008) for the uniform vegetation. In order to achieve a more realistic dependency of this process in the three vegetation zone scheme, we now approximate a mean atmosphere temperature for each vegetation zone separately by making use of the DCESS model latitudinal temperature profile expressed as a second order Legendre polynomial in sine of latitude (Shaffer et al., 2008). This yields,

$$T_{TF} = \frac{(T_{atm,LL} - 0.5 \cdot T_{atm,HL}) \cdot sin(L_{TF-GSD}) + 0.5 \cdot T_{atm,HL} \cdot sin(L_{TF-GSD})^3}{sin(L_{TF-GSD})}, \tag{11}$$

$$T_{GSD} = \frac{(T_{atm,LL} - 0.5 \cdot T_{atm,HL}) \cdot (sin(L_{GSD-EF}) - sin(L_{TF-GSD})}{sin(L_{GSD-EF}) - sin(L_{TF-GSD})}$$
$$+ \frac{0.5 \cdot T_{atm,HL} \cdot (sin(L_{GSD-EF})^3 - sin(L_{TF-GSD})^3)}{sin(L_{GSD-EF}) - sin(L_{TF-GSD})} \tag{12}$$

and

$$
\begin{aligned}
T_{EF} \;=\; & \frac{(T_{atm,LL} - 0.5 \cdot T_{atm,HL}) \cdot (sin(L_{snow/ice}) - sin(L_{TF-GSD}))}{sin(L_{snow/ice}) - sin(L_{TF-GSD})} \\
& + \frac{0.5 \cdot T_{atm,HL} \cdot (sin(L_{snow/ice})^3 - sin(L_{TF-GSD})^3)}{sin(L_{snow/ice}) - sin(L_{TF-GSD})}.
\end{aligned}
\tag{13}
$$

Here, $T_{atm,LL}$ denotes the mean atmosphere temperature in the DCESS model low-mid latitude sector ($0° - 52°$) and $T_{atm,HL}$ in the model high latitude sector ($52° - 90°$). $L_{snow/ice}$ stands for the minimum of the latitude of the snow and the ice sheet line (see next section). Now, λ_Q, which influences the decay of litter and soil, can be calculated for each vegetation zone separately with $\lambda_Q^i \equiv Q_{10}^{(T^i - T_{PI}^i)/10}$, where the index $i = 1, 2, 3$ stands for the three vegetation zones TF, GSD and EF. The conservation equations for the land biosphere reservoirs of ^{12}C from Shaffer et al. (2008) for leaves (M_G), wood (M_W), litter (M_D) and soil (M_S) thus split into twelve equations, four for each vegetation zone:

$$
\frac{dM_G^i}{dt} = \frac{35}{60} \cdot NPP^i - \frac{35}{60} \cdot NPP_{PI}^i \cdot \frac{M_G^i}{M_{G,PI}^i}
\tag{14}
$$

$$
\frac{dM_W^i}{dt} = \frac{25}{60} \cdot NPP^i - \frac{25}{60} \cdot NPP_{PI}^i \cdot \frac{M_W^i}{M_{W,PI}^i}
\tag{15}
$$

$$
\frac{dM_D^i}{dt} = \frac{25}{60} \cdot NPP^i \frac{M_G^i}{M_{G,PI}^i} + \frac{20}{60} \cdot NPP_{PI}^i \cdot \frac{M_W^i}{M_{W,PI}^i} - \frac{55}{60} \cdot NPP_{PI}^i \cdot \lambda_Q^i \cdot \frac{M_D^i}{M_{D,PI}^i}
\tag{16}
$$

$$
\frac{dM_S^i}{dt} = \frac{5}{60} \cdot NPP^i \frac{M_W^i}{M_{W,PI}^i} + \frac{10}{60} \cdot NPP_{PI}^i \cdot \lambda_Q^i \cdot \frac{M_D^i}{M_{D,PI}^i} - \frac{15}{60} \cdot NPP_{PI}^i \cdot \lambda_Q^i \cdot \frac{M_S^i}{M_{S,PI}^i}
\tag{17}
$$

Analogously, these equations are extended for the rare carbon isotopes ^{13}C and ^{14}C, where fractionation factors for land photosynthesis and, for ^{14}C, radioactive sinks are considered (Shaffer et al., 2008). The flux of carbon dioxide between the terrestrial biosphere and the atmosphere is then determined by

$$
F_{CO_2} = \sum_{i=1}^{3} -NPP^i + \frac{45}{55} \cdot \frac{dM_D^i}{dt} M_D^i + \frac{dM_S^i}{dt} M_S^i.
\tag{18}
$$

As indicated above, M_D^i and M_S^i represent the biomass carbon reservoirs in litter and soil for the different vegetation zones, respectively, and dM_D^i/dt and dM_S^i/dt their decay rates. For the two rare carbon isotopes, additionally the corresponding fractionation factors $^{13,14}\alpha$ have to be considered. The flux is then given by

$$
F_{^{13,14}CO_2} = \sum_{i=1}^{3} -NPP^i \cdot \frac{^{13,14}C}{^{12}C} \cdot {}^{13,14}\alpha + \frac{45}{55} \cdot \frac{dM_D^i}{dt} \cdot {}^{13,14}M_D^i + \frac{dM_S^i}{dt} \cdot {}^{13,14}M_S^i.
\tag{19}
$$

2.3 Formulation of permafrost

On glacial-interglacial time scales, global temperature changes lead to terrestrial ice sheet advances and retreats. These can cover large parts of the terrestrial biosphere and thereby prevent land-atmosphere carbon exchange in these areas. In the DCESS model, we account for this by introducing the parameter L_{ice}, that limits the poleward extent of the BF vegetation zone.

5   During interglacials, when ice sheets retreat to about $70°$ latitude, this limitation is determined by the extent of permafrost, characterised by the parameter L_{snow} that is defined as the latitude of $0°C$ global mean temperature. Hence, the minimum of these two parameters ($L_{snow,ice} = min(L_{snow}, L_{ice})$) at the current time step is used to determine the limitation of the BF vegetation zone. When $L_{snow/ice}$ advances and retreats on large spatial scales, organic carbon is buried/released below/from permafrost areas or terrestrial ice sheets. That means, additional land-atmosphere carbon (^{12,13,14}C) flux variations due to the

10   changes of permafrost area are considered. For this, we add the permafrost flux term $^{12,13,14}F_{CO_2,PF}$ to Eqs. 18 and 19, which is calculated by

$$^{12,13,14}F_{CO_2,PF} = \frac{dA_{snow/ice}}{dt} \cdot ^{12,13,14}C_{PF}. \tag{20}$$

$$\frac{dA_{snow/ice}}{dt} = 2\pi R \cdot \left[\left(1 - \frac{270}{360}\right) \cdot \left((1 - sin(L_{snow/ice}^{t})) - (1 - sin(L_{snow/ice}^{t-1}))\right) \right] \tag{21}$$

15   and denotes the change in snow or ice covered area. For this, $L_{snow/ice}$ of the previous $(t-1)$ and the current (t) time step is taken. R denotes the Earth radius and the factor $(1 - 270/360)$ takes account for the land fraction in the model geometry.

   $^{12}C_{PF}$, the amount of carbon being stored in permafrost, was approximated to $30\,kg \cdot m^{-2}$ by Schuur et al. (2015). For the stable $^{13}C_{PF}$ isotope, carbon is buried and released through permafrost with the same isotope ratio. We hence set the value to $0.33\,kg \cdot m^{-2}$, to yield a, in our simulations, typical isotope ratio for EF soil of $\delta^{13}C = -24‰$ (Zech (2012) estimates this

20   value to $-27‰$). For $^{14}C_{PF}$, however, radioactive decay ($T_{1/2}(^{14}C) \approx 5730\,a$) across glacial periods, when large parts of the high latitudes are covered by terrestrial ice sheets, has to be considered. While being buried with the current isotope ratio of soil, we therefore assume carbon to be released from permafrost radiocarbon free ($\Delta^{14}C = -1000‰$). This has also been considered to be reasonable by Zech (2012) for the last deglaciation. As is, the land area of the model simply covers 1/4 of the globe from the equator to 70 degrees latitude. In our configuration for the last glacial termination, permafrost affects latitudes

25   between $47°$ and around $54°$ (see Fig. S3 in the Supplement). Across these latitudes, the land fraction averaged over both hemispheres is around 30% (see e.g. Matney, 2012). Thus, a further adjustment for the permafrost effect due to land fraction was not considered to be necessary.

2.4 Evaluation of the new module

As a test of to what extent the newly developed land biosphere scheme adequately represents the behaviour of the different

30   vegetation zones for global climate changes, we now present a more detailed evaluation of a cooling simulation. For this purpose, we show the response of the model vegetation zones and the different vegetation reservoirs to a reduction of atmospheric

temperatures and pCO$_2$ to LGM conditions. Moreover, we compare the results with complex vegetation models as well as with data reconstructions.

To evaluate the vegetation scheme for LGM conditions, we carried out cooling simulations with the new and with the old biosphere scheme. For these, we started from a PI steady-state, but prescribed the global mean temperature to T$_{glob}$=11.5 °C
5 (see Shakun et al., 2012) and the atmospheric pCO$_2$ concentration to 190 ppm (e.g. Monnin et al., 2001). Fig. 3a shows the global sum of total land biomass (LB) carbon for the two cooling simulations as well as LB carbon for the three individual vegetation zones and Fig. 3b shows LB carbon of the vegetation reservoirs above ground (leaves + wood) and below ground (litter + soil) for the two simulations. Since the system seems to be in equilibrium after around 1 ka, we integrated these simulations over 2 ka.
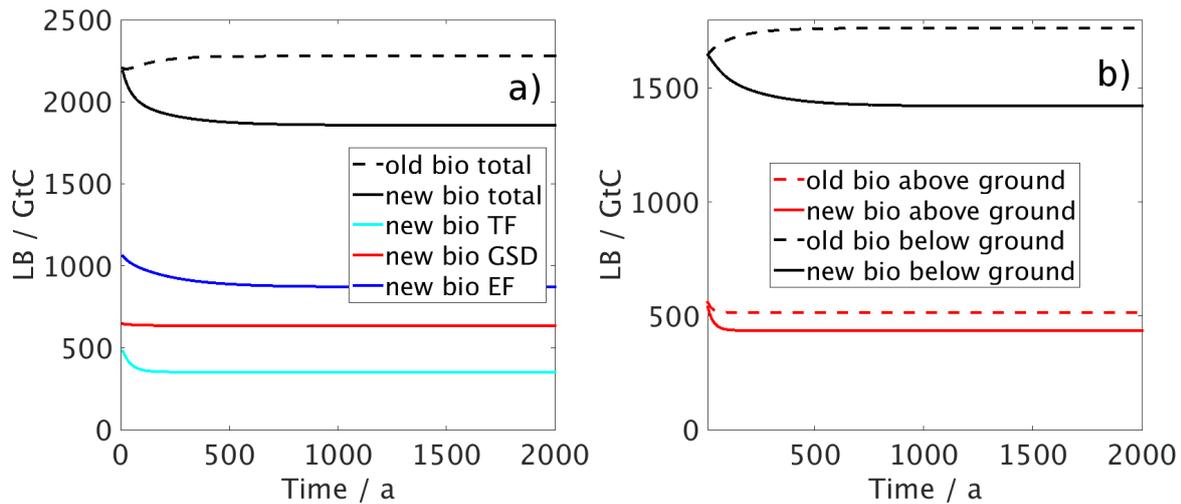
Figure 3. Cooling simulation (see text) for the model version with the new (solid) and the old (dashed) vegetation scheme. a) Total land biomass carbon (in black) and separated into the three vegetation zones (TF: cyan, GSD: red, EF: blue) for the new vegetation scheme. b) Land biomass carbon separated into the reservoirs above ground (leaves + wood) in red and below ground (litter + soil) in black.

10 As already presented in Fig. 1, the cooling experiment again demonstrates that LB carbon increases in the old model version and decreases with the new biosphere scheme. Fig. 3b shows that the unrealistic increase of LB carbon is mainly due to an increase in litter/soil carbon. In the simulation with the new biosphere scheme, this does not happen, mainly because of the limitation of the poleward expansion of the EF zone through the snow line. A poleward limitation of the biosphere in the old scheme also leads to a reduction of LB carbon in the cooling simulation. To confirm this, we performed an additional simulation
15 with the old vegetation scheme, but with a crude vegetation area limiting approach $A = (sin(L_{snow})/sin(L_{snow,PI}))^2$. In this cooling experiment, the total LB carbon decreases, but not as much as with the new biosphere and the decrease happens faster than with the new biosphere scheme (not shown). The LB change in the EF zone mainly depends on variations in soil, which has a slow response time and is the largest biomass reservoir (Fig. 3a). The TF zone adapts much quicker to the new climate

conditions because in this vegetation type the biomass is dominated by leaves and wood. The GSD vegetation zone shows the smallest change in biomass, because in the cooling simulation the area of this vegetation zone changes only slightly, but rather just shifts latitudinally.

We calibrated the latitudinal dependency of the vegetation zone borders to match the LPJ model results. However, the calculation of carbon stored in the terrestrial biosphere at different climate conditions also depends on other parameters. Hence, we also evaluate the performance of the new DCESS vegetation scheme by comparing it to the results of the LPJ model study by Gerber et al. (2004). For this, Tab. 2 shows the percentual change of biomass carbon in the cooling experiment with the new and the old DCESS model version, as well as for the old version with the biosphere area limit (old bio plus) and the LPJ model.

ΔLB / %	Total	Litter + Soil	Leaves + Wood
Old bio	+3.0	+9.5	−14.5
Old bio plus	−10.8	−5.2	−26.0
New bio	−18.0	−14.2	−28.5
LPJ	−24.8	−24.7	−25.0

Table 2. Percentual change of biomass carbon in the cooling experiment for total biomass and divided into reservoirs above and below ground. DCESS model with old and with new biosphere scheme and LPJ model study presented in Gerber et al. (2004).

This comparison demonstrates that in relation to the LPJ model, the adaptation of the LB to different climate conditions is captured much better with the new biosphere scheme. While with the old model version, biomass carbon increased, the new biosphere scheme produces most of the change that the LPJ model shows. Most of the improvement in LB variations through the new vegetation scheme is due to the snow line, that limits the poleward expansion of the biosphere. Using the old biosphere with additional vegetation area limitation, LB carbon decreases under LGM climate conditions. However, with the new vegetation scheme, the snow line particularly limits the EF zone, which is dominated by litter and soil and this largely improves the overall representation of biomass below ground. When vegetation area reduction was applied to the old biosphere module, the biomass change above ground was already in good agreement with the LPJ model. Hence, the reason for the much larger changes in overall biomass between the old and the new model version as shown in Fig. 3 is mainly due to the better representation of the slow change of the soil biomass in the EF zone. This more accurate representation of soil in the EF zone, however, is also due to the fact that now the biomass reservoir of each vegetation zone depends on the specific temperature of the zone in question and not on the global mean temperature as in the old model version.

Peng et al. (1998) provide an overview of various studies that estimate the reduction in global land biomass for the LGM compared to present day. Those are based on either global circulation model (GCM) simulations, marine carbon isotope data changes or vegetation mapping approaches. Altogether, these studies show a large spread from 0 (Prentice and Fung, 1990) to $-1350\,GtC$ (Adams et al., 1990). The majority of the studies show values between -300 and $-700\,GtC$, a more recent

modelling study by Prentice et al. (2011) provides values of -550 to $-694\,GtC$. Through the implementation of the new vegetation scheme, the DCESS model biomass carbon change between PI and LGM does improve from $+43$ to $-408\,GtC$. Thus results with the new model version agree well other estimates, albeit at their low end.

Overall, it can be stated that the new biosphere scheme with the three vegetation zones constitutes a significant improvement for the representation of the terrestrial biomass as well as the estimates of the size and timing of carbon exchanges between the terrestrial biosphere and the atmosphere. This new implementation better captures the complex interactions between the terrestrial and the atmospheric carbon exchange as is required for a better understanding of the processes that determine climate changes on glacial-interglacial time scales.

3 Application to Last Glacial Maximum and deglaciation

As a first application of the new DCESS terrestrial biosphere module, we simulate the deglaciation after the LGM, when global atmospheric temperatures rose by around $3.5\,K$ (Shakun et al., 2012) and atmospheric pCO_2 increased from $190\,ppm$ during the LGM to Holocene conditions of $260\,ppm$ in a series of steps (e.g. Monnin et al., 2001). The most marked of these steps is a steep $38\,ppm$ rise near the onset of the deglaciation, the Mystery Interval (Broecker and Barker, 2007). In the Supplement, we provide a literature review with details about the Mystery Interval including current hypotheses for the explanation of that climate change.

A complete explanation for the pCO_2 and temperature increase at the onset of the last glacial termination must be able to reproduce a simultaneous decrease by $0.3‰$ and $160‰$ of atmospheric $\delta^{13}C$ (Schmitt et al., 2012) and $\Delta^{14}C$ (Reimer et al., 2013), respectively. Furthermore, it should also include how LGM deep water with high salinity (Adkins et al., 2002), low $\delta^{13}C$ (Curry and Oppo, 2005) and $\Delta^{14}C$ (Burke and Robinson, 2012) and low dissolved oxygen concentrations (but not widespread anoxia) (Jaccard et al., 2014) was formed during the last glacial. Hence, it requires the consideration of a globally comprehensive picture of the physical and biogeochemical processes in atmosphere, ocean and on land, as well as their interactions on various time scales. With its new biosphere scheme, the DCESS model is now better suited for investigations of that kind. However, a number of further adaptions need to be made to simulate LGM conditions and the transition to the Holocene. These are presented next followed by transient simulations across the last $25\,kaBP$. For these, the model was initialised and forced with the conditions described in Sect. 3.1. Since we focus on the MI ($17.5 - 14.5\,kaBP$), we mainly present and discuss the time period from 20 to $10\,kaBP$. We assess the impact of various processes on the overall climate change with a focus on the new biosphere scheme and permafrost. In the process, we also evaluate proposed time series for the production of ^{14}C in the atmosphere.

3.1 Model Last Glacial Maximum and transition

Guided by proxy-data records, we first modified several biogeochemical and physical parameters to generate a model steady-state that represents the LGM well. For this, a number of parameters can be considered as possible candidates (see e.g. Kohfeld and Ridgwell, 2009). However, under consideration of the possibilities provided by the enhanced model and knowledge about
5 candidate parameters, we decided upon the adaptions described below.

Increased iron supply and thereby ocean fertilisation (Martin et al., 1990) through enhanced atmospheric dust concentrations during the LGM (see e.g., Mahowald et al., 1999, 2006b; Maher et al., 2010), particularly in the high southern latitudes (e.g. Lambert et al., 2013, 2015), probably led to enhanced new production of organic matter in the Southern Ocean (SO) by way of iron fertilization (see also Lamy et al., 2014; Martínez-García et al., 2014). To account for this, we modified the efficiency factor
10 for new production in the model high latitude ocean sector from 0.36 (standard value for PI conditions, see Shaffer et al., 2008) to 0.5. This leads to a reasonable productivity increase of around 40% for the area of the SO and induces an atmospheric pCO$_2$ reduction of around 20 ppm, consistent with the DCESS model iron fertilisation results in Lambert et al. (2015). Moreover, an additional radiative effect of $-1\,Wm^{-2}$ (Mahowald et al., 2006a) for glacial conditions through atmospheric dust during the LGM is considered. For the transient simulations from the LGM to the Holocene, we have developed a transfer function
15 between temperature and dust fluxes from proxy data records that we applied to the efficiency factor and to the radiative effect. It yielded an exponential dependency of dust with temperature; details can be found in the Supplement.

The lower sea level during the LGM (around 130 m, see e.g., Waelbroeck et al., 2002; Lambeck et al., 2014) and a thereby reduced ocean volume by around 3.5% (see e.g. Adkins and Schrag, 2002) is accounted for by increasing phosphate concentrations (the nutrient limiting source in the DCESS ocean biochemistry) and the ocean salinity (see Adkins et al., 2002) by 3.5%.
20 For the transition of these parameters across the last 25 kaBP, we use the latest sea level reconstruction time series from Lambeck et al. (2014). To generate LGM conditions for Δ^{14}C in atmosphere and ocean, we applied the average cosmogenic ^{14}C production rate from 25 to 26 kaBP ($PR_{14C} = 2.1 \cdot 10^4\,\text{atoms/cm}^2\text{s}$). For this and in most of the transient simulations, we use the most recent production rate time series developed by Hain et al. (2014). In a sensitivity analysis, the ^{14}C production rates from the studies by Laj et al. (2004) and Muscheler et al. (2004) are applied as well. A description of the main characteristics
25 of these data is given in the Supplement.

The equatorward expansion of terrestrial ice sheets is set to 47° latitude for generating LGM conditions. This is within the uncertainty range of LGM climate reconstructions (see e.g. Peltier, 2004) and has to be understood as a global two hemisphere average. For the transient simulations, we impose the temporal retreat of the ice line to the disappearance of the ice sheets at 70° latitude during the Holocene. For this, we linearly prescribe L$_{ice}$ (see Sects. 2.2 and 2.3) to a data set presented in Shakun
30 et al. (2012) showing the Northern Hemisphere (NH) ice sheet expansion from 100% (ice line at 47°) at the LGM to 0% (ice line at 70°) at present day. An example case for L$_{ice}$ and L$_{snow}$ in a transient simulation is given in the Supplement.

A model analogy to isolated deep water in the SO (see e.g. Watson and Naveira Garabato, 2006) is generated through application of a depth-dependent function for vertical exchange intensity in the high latitude ocean sector. For this, we impose a sharp decrease in vertical diffusion at around 1800 m ocean depth which limits mixing of the upper ocean layers with

intermediate and deep ocean waters. The transition depth of this profile was varied to obtain LGM climate conditions that constrain all required oceanic and atmospheric variables. Through the application of this diffusivity profile, the isolated ocean waters below the transition change towards high dissolved inorganic carbon (DIC) and alkalinity values as well as towards low oxygen concentrations and ^{13,14}C isotope ratios. This variation in vertical exchange intensity should not be understood as a

5 change in real oceanic vertical diffusion, but rather as a model analogy for LGM conditions of the SO that were likely due to some combination of weakened or equatorward shifted westerly winds (Toggweiler and Russel, 2008; Anderson et al., 2009; d'Orgeville et al., 2010) and increased stratification through brine-induced effects (Bouttes et al., 2010, 2011; Mariotti et al., 2013). With its wide latitudinal extent and the land bounding poleward of $70°$, the high latitude ocean sector of the DCESS model bears considerable resemblance to the SO. During the transient simulations, we slowly restore this modification back

10 toward PI conditions between 17.5 and 14.5 kaBP to apply the entire effect of this process to the MI. In this process, deeper layers in the high latitude ocean sector are again brought in contact with surface layers promoting outgassing and ocean profiles go back toward the initial PI state shown in Shaffer et al. (2008). An illustration of the profile as well as a detailed technical description of the procedure and some additional information are presented in the supplementary material.

When all these adaptations, plus a few minor changes (described in the Supplement), are applied, an 80 ka DCESS simulation

15 leads to a steady climate state with conditions close to data-based LGM reconstructions. Atmospheric pCO_2 decreases to 187.9 ppm and the global mean atmosphere temperature to $11.70\,°C$. For pCO_2, proxy data records by Lüthi et al. (2008) provide a range of $186 - 198$ ppm and Shakun et al. (2012) present LGM global mean atmosphere temperatures between 11.5 and $11.8\,°C$. Moreover, atmospheric isotope ratios of $\delta^{13}C = -6.41‰$ and $\Delta^{14}C = 414.5‰$ and low oxygen values but no widespread anoxia in the deep ocean are achieved. This agrees well with proxy data records presented by Schmitt et al. (2012)

20 and Reimer et al. (2013). An overview of these data and the ocean profiles for LGM conditions of various variables for the high and the low-mid latitude sector are shown in the Supplement. In the following sections, we present analyses of the transient simulations from the LGM to the Holocene, using the transition functions described above.

3.2 Transient simulation results

Four transient simulations have been conducted to assess the impacts of the individual transition functions on atmospheric

25 T_{glob}, pCO_2, $\delta^{13}C$ and $\Delta^{14}C$ changes. The transition functions described above were applied sequentially to better assess the impact of each process. These simulations show that during the 3 ka of the MI, all the above described processes together generate a change of 18 ppm pCO_2, $0.8\,°C$ global temperature, $-0.18‰$ $\delta^{13}C$ and $-85‰$ $\Delta^{14}C$ (see Supplement). This is only about half of the change that data-based reconstructions show. Most of the simulated changes can be attributed to the resumption of the ocean high latitude vertical diffusion and the thereby induced outgassing of the carbon-rich and isotopically

30 depleted deep waters. Our DCESS simulations reproduce some aspects of the early last deglaciation, while others are still underestimated because important processes are either missing or not adequately represented.

In order to evaluate how much influence permafrost has on the atmospheric quantities, we now deactivate the permafrost in the computation of the atmosphere-terrestrial biosphere fluxes (No_PF, **no** influence of **p**erma**f**rost). For this, we set the additional permafrost-atmosphere carbon (including the rare isotopes) fluxes to zero throughout the simulation with all changes

(the All_TF simulation, see Supplement). Fig. 4 shows the results of these simulations and moreover, those of a simulation with the same conditions, but with the old uniform land biosphere scheme (Old_bio) which does also not feature the parameterisation for permafrost. It does, however, have the snow/ice line-based reduction of biosphere area included that was presented in Sect. 2.4. Old_bio (use of the **old bio**sphere module) is included in this figure to evaluate the general influence of the vegetation zones and the permafrost on the simulation.
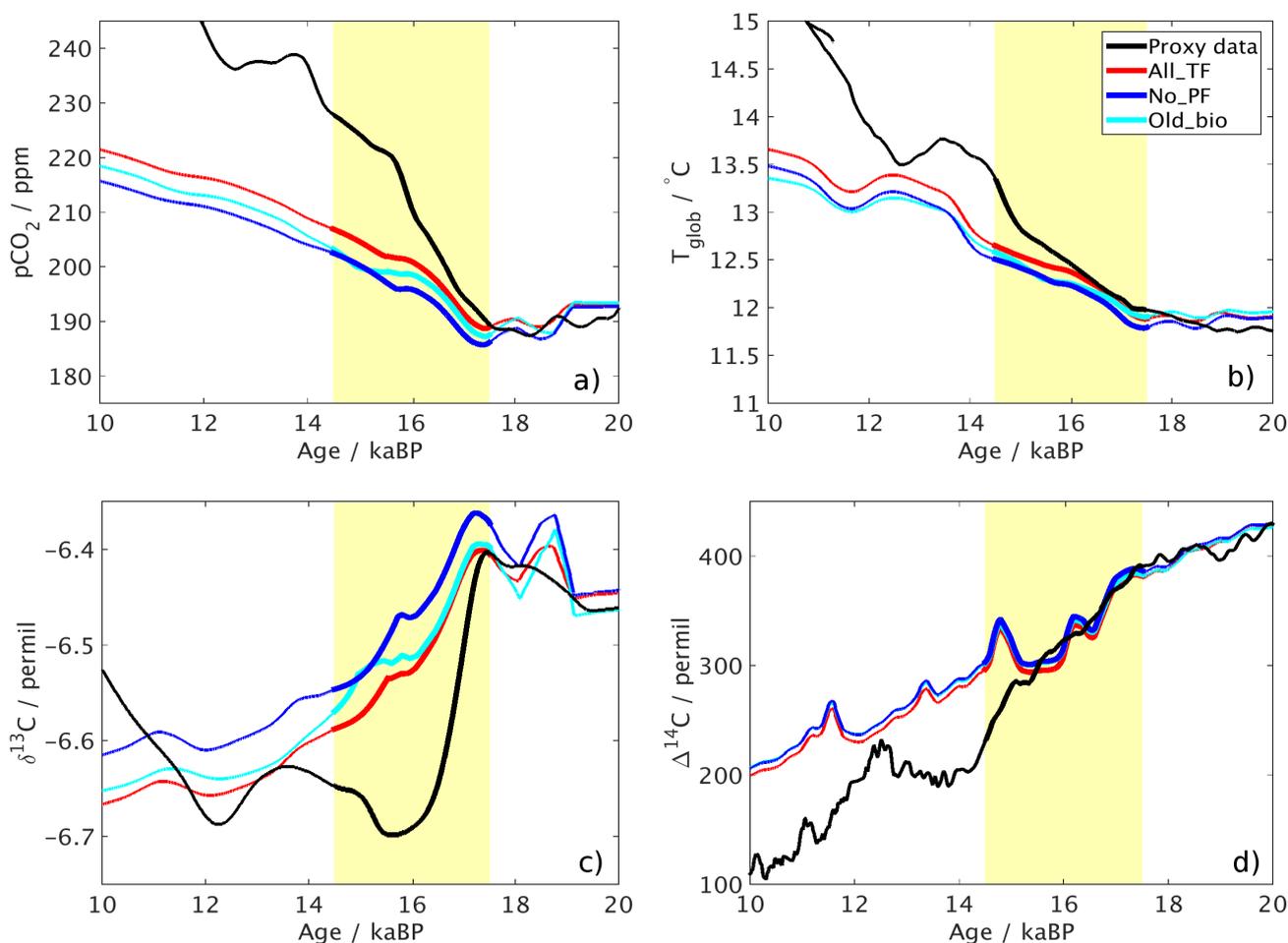
Figure 4. Atmospheric values for the DCESS simulation with all transition functions (All_TF, red line, see Supplement) and data-based reconstructions (black); pCO_2 by Lüthi et al. (2008), temperatures by Shakun et al. (2012), δ^{13}C by Schmitt et al. (2012) and Δ^{14}C by Reimer et al. (2013). Blue line: DCESS simulation with all transitions functions, but deactivated permafrost component (No_PF). Cyan line: Same simulation with the old terrestrial biosphere scheme (Old_bio).

In the simulation without the influence of permafrost, a reduction of the change across the MI can be observed in all four atmospheric variables compared to the reference simulation All_TF. The results of the two simulations start diverging at

around 19 kaBP. This is when the change in ice sheet extent leads to first clear variations through its effect on the permafrost parameterisation in the model (see Fig. S4 in the Supplement). Across the MI, the difference between the two lines additionally increases in all four panels and only slightly thereafter. Until the year 14.5 kaBP, the permafrost component accounts for an additional change of around 2.6 ppm in pCO_2 (6.8% of the 38 ppm change during the MI), about 0.1 °C in global mean atmosphere temperature, and only $-0.01‰$ in $\delta^{13}C$ and $-2‰$ in $\Delta^{14}C$. This indicates, that for the overall climate change across the MI, permafrost plays only a secondary role, with relatively small contributions to temperature and isotopes. $\Delta^{14}C$ is not sensitive to changes in vegetation and hence the influence of its release from permafrost dominates its development.
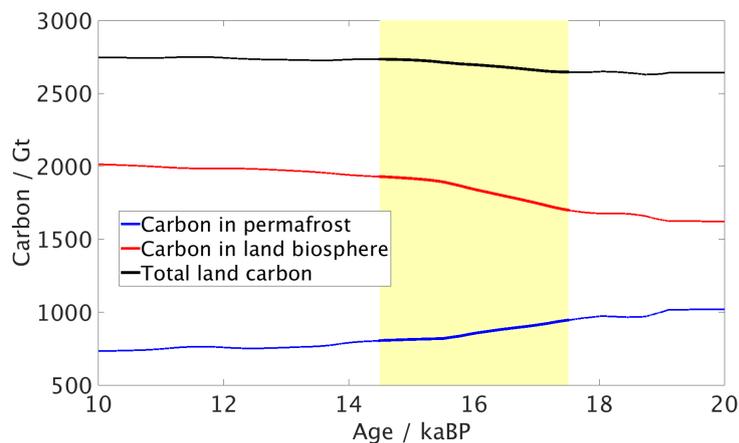
Figure 5. Carbon stored in soil below permafrost and in the terrestrial biosphere as well as their sum for the All_TF simulation.

Fig. 5 shows the changes of permafrost carbon, land biosphere carbon and their sum for the All_TF simulation. In this simulation, carbon uptake through the regrowth of the biosphere across the MI slightly exceeds (by 70 GtC) carbon outgassing through ice sheet retreat and permafrost thawing then. This demonstrates that the two mechanisms actually broadly compensate each other. Each of these changes, however, is subject to considerable uncertainty. As mentioned above, the land biosphere carbon reservoir change in the model is at the low end of the range found in other studies (Peng et al., 1998; Prentice et al., 2011). Also, model carbon release of 337 GtC from permafrost is lower than that of Ciais et al. (2012), who found a 700 GtC difference between LGM and present day global permafrost carbon reservoir. Our lower estimate may be related to our simplified permafrost treatment that used estimates of the extent of land area covered by ice sheets as well as the simple assumption of 30 kg of available carbon per square meter of permafrost covered area (Schuur et al., 2008).

As has been mentioned above, the change in $\Delta^{14}C$ during the MI in the All_TF simulation is not as large as in the data-based reconstructions. Apart from atmospheric CO_2 itself and the release of deep ocean waters, $\Delta^{14}C$ is strongly influenced by the cosmogenic production rate of ^{14}C. This production rate is determined with rather large uncertainties and there are different ways to derive it. In the Supplement, we present the three ^{14}C production rate time series of the studies by Laj et al.

(2004); Muscheler et al. (2004) and Hain et al. (2014) across the last 25 kaBP. Here, we present an evaluation of the three ^{14}C production rate data applied to the ALL_TF simulation. In Fig. 6, we show the simulations with the three different production rates, as well as for a simulation with constant LGM-value production rate (Mus_PR, Muscheler et al. (2004) **p**roduction **r**ate; Laj_PR, Laj et al. (2004) **p**roduction **r**ate; LGM_PR, constant **LGM**-value **p**roduction **r**ate). The proxy data record by Reimer et al. (2013) is also included in the figure.
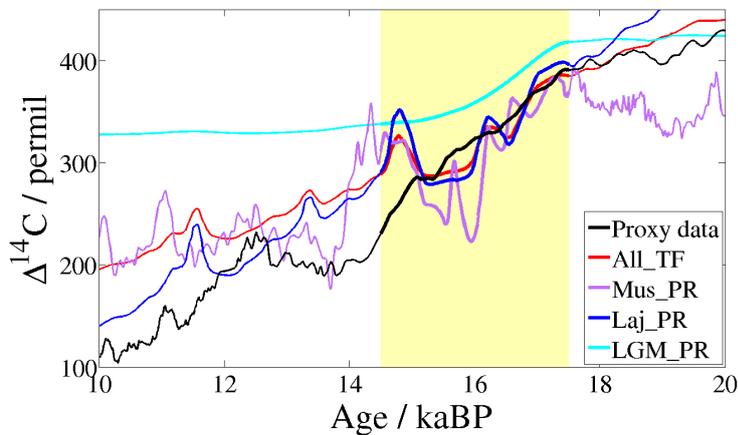
Figure 6. Δ^{14}C in transient simulations with all changes (see Sect. 3.1) applying different ^{14}C production rates from Muscheler et al. (2004) (magenta, Mus_PR) Laj et al. (2004) (blue, Laj_PR), Hain et al. (2014) (red, All_TF) and fixed LGM production rate (cyan, LGM_PR), and data based reconstructions from Reimer et al. (2013) (black).

The simulation with constant ^{14}C production rate at LGM level shows a Δ^{14}C drop by 80‰ from the beginning to the end of the MI, almost entirely through the outgassing of isotopically depleted deep ocean waters. Neither of the ^{14}C production rates can account for the remaining 80‰ reduction to explain the Δ^{14}C decrease of 160‰ across the MI that can be seen in the data-based reconstruction by Reimer et al. (2013). With the data set by Hain et al. (2014), Δ^{14}C drops by 96‰, using the Laj et al. (2004) data, a 105‰ decrease can be explained and the Muscheler et al. (2004) time series only leads to -58‰ change. Furthermore, the proxy data does not show the production rate-caused variations within the MI and also, in the Mus_PR simulation, atmospheric Δ^{14}C shows a large and sudden drop of around 150‰ shortly after the MI between 14.3 and 13.7 kaBP.

3.3 Discussion of transient simulations

The model reproduces around half of the MI changes in atmospheric pCO$_2$, T$_{glob}$, δ^{13}C and Δ^{14}C as shown in data-based reconstructions. Most of these changes are caused by the upward transport of carbon-rich and isotopically depleted waters from the deep ocean through prescription of the vertical diffusion profile and its resumption, but also other processes play important roles. The dust component accounts for about 0.3 °C global temperature change during the MI. Since the other atmospheric quantities are only moderately affected by dust, most of that is can be related to the direct dust radiative forcing.

The δ^{13}C drop at the onset of the deglaciation is fairly well represented by this DCESS modelling approach and also mainly caused by deep ocean mixing. Also Brovkin et al. (2002) point out the importance of oceanic processes for atmospheric δ^{13}C at glacial-interglacial time scales. However, after around 12 kaBP, δ^{13}C increases again in the observations, while it remains relatively constant in the simulations. Schmitt et al. (2012) mainly attribute this rise to the continuing regrowth of the land
5   biosphere, which does not have such a strong effect on atmospheric δ^{13}C in the model. According to Crichton et al. (2016), also peatlands could account for this effect, those however, are not included in our vegetation scheme.

The impact of permafrost on Δ^{14}C is very small, even though we assume carbon released from permafrost to be radiocarbon free. The expected radiocarbon decrease generated through permafrost thawing can apparently be compensated by ocean-atmosphere exchange and subsequent mixing to the deeper ocean. It has to be considered that the carbon buried below
10 permafrost seems to be underestimated in our model approach compared to a study by Ciais et al. (2012) and that interhemispheric see-saw effects can affect the timing of extensive permafrost (^{14}C depleted) carbon release, especially during HE1 (see e.g. Köhler et al., 2014). The much discussed sharp Δ^{14}C drop of 160‰ (see Reimer et al., 2013) (note that in previous studies by Broecker and Barker (2007) or Reimer et al. (2009) this was referred to as 190‰) at the early stages of the last deglaciation is not entirely reproduced by this modelling study. By applying a constant LGM ^{14}C production rate, all the above described
15 processes can account for about 70‰ change. None of the three different time series of the ^{14}C production rate can account for the rest of the Δ^{14}C change. At most, the data by Laj et al. (2004) leads to an additional 25‰ decrease. However, the determination of the ^{14}C production rate is obviously subject to large uncertainties. For example, the drop in the Muscheler et al. (2004) time series at around 14 kaBP leads to a sudden 150‰ decrease in Δ^{14}C in our model simulation but can not be seen in Δ^{14}C proxy data. In this context, it should be mentioned, that recent revisions to ice core time scales have not yet
20 been applied for revising the reconstructed snow accumulation rates and ^{10}Be fluxes and its influence on the ^{10}Be-based ^{14}C production rate (R. Muscheler, personal communication, 2015).

To account for the other half of changes that our simulations can not reproduce, several processes can be thought of being insufficiently represented in the model and moreover, this could also be due to the timing of one or more of the transition functions, underrepresenting effects during the MI. Brovkin et al. (2007); Kohfeld and Ridgwell (2009) and Mariotti et al.
25 (2013) discuss a number of processes that combined can account for the entire deglaciation, although with sometimes large uncertainties, not all of them were captured in our study. E.g., enhanced ocean remineralisation length scales during the glacial, due to less active bacteria at low temperatures, could trap more DIC in the deep ocean, which then could account for additional CO_2 outgassing but would also reduce deep ocean dissolved oxygen concentrations. Also the volume of isolated deep waters in the SO is uncertain and moreover, water masses in other oceans may also have contributed to the overall atmospheric pCO_2
30 change (Rose et al., 2010; Okazaki et al., 2010; Kwon et al., 2012; Huiskamp and Meissner, 2012). The T_{glob} and pCO_2 changes after the MI across the BA, the Younger Dryas and the Holocene are not expected to be simulated in detail by the DCESS model. Due to the model's simplified geometry, interactions between the hemispheres and thus the bipolar seesaw can not be represented. The simplicity of DCESS model ocean dynamics also limit feedbacks of ocean-atmosphere interactions that may have contributed to the overall carbon cycle change during the MI. For instance, Mariotti et al. (2016) discuss the effect
35 of North Atlantic freshening through ice sheet melting inducing upper water stratification and subsequent prevention of carbon

uptake by the ocean to contribute to enhanced pCO_2 during HE1 at the end of the MI. An alternative approach would be to use 3-D modelling to deal specifically with one or more of the processes listed above. However, this would involve other types of uncertainties like the strength and position of the Southern Westerly Winds and the parameterisation of diapycnal mixing.

4 Summary and conclusions

The land biosphere scheme that accounts for $^{12,13,14}C$ cycling with leaf, wood, litter and soil of the reduced complexity Earth System Model DCESS has been extended to three different vegetation zones. Based on a complex land biosphere model study, we defined dynamically varying vegetation borders on a global scale that depend on temperature variations. We also introduce a parameterisation that accounts for carbon, including its rare isotopes, that is being trapped below the permafrost as well as below terrestrial ice sheets for glacial conditions and released during deglaciation events. In an evaluation, the new terrestrial biosphere scheme is shown to simulate more realistic global biomass size and timing in climate change experiments, and thereby significantly improves the representation of land-atmosphere carbon exchange rates in the DCESS model. For climate change studies on glacial-interglacial time scales, these aspects can be crucial when analysing the contributions and interactions of processes controlling carbon exchange between land, atmosphere and ocean.

For a first application of the new biosphere parameterisation, the model is first tuned to Last Glacial Maximum conditions to subsequently carry out transient simulations across the last glacial termination. Along with a number of established adaptations of physical and biogeochemical parameters, the DCESS model successfully reproduces proxy data records of glacial conditions in the ocean and atmosphere when we impose the isolation of high latitude deep ocean waters. For the transient model simulations, we have additionally developed a set of explicit functions that describe the transitions of atmospheric dust, ocean volume and terrestrial ice sheet extent across the last 25 kaBP. These sensitivity eperiments show that large parts of the exceptional change in atmospheric pCO_2, $\delta^{13}C$, $\Delta^{14}C$ and T_{glob} at the onset of the last glacial termination (Mystery Interval, 17.5-14.5 kaBP) can be represented by this approach. Some variations as seen in data-based reconstructions can not be reproduced by our model study. These remaining changes could possibly be captured by applying a dynamically more complex model including distinct water masses and a second hemisphere for representing bipolar seesaw effects, or by revising and/or adding one or more model parameterisations. New insights into these mechanisms can help to improve our understanding of global carbon cycle changes on centennial to millennial time scales.

The thawing of permafrost due to atmospheric warming and retreat of ice sheets, as well as the regrowth of the terrestrial biosphere, are found to play moderate, but important roles in explaining the climate change of this period of the last deglaciation. We found that these two processes broadly compensate each other in the model in terms of CO_2 exchange with the atmosphere, making little net contribution to atmospheric pCO_2 changes across the last transition. Simulations across the transition using the original DCESS land biosphere model also showed essentially no net contribution to atmospheric pCO_2 change as reflected in the very small change in land biomass between LGM and present day. But with the new biosphere module (including permafrost) this result is obtained in a more correct manner, in better agreement with proxy data and more complex modelling results.

Supplementary material related to this article is available online at doi:10.5194/gmd-0-1-2016-supplement.

Code and data availability: The DCESS model code is available at http://www.dcess.dk/ and all applied data are available as referenced.

Acknowledgements. We thank Raimund Muscheler for providing ^{14}C production rate data and information about it as well as Ricardo De
5 Pol-Holz for discussions. This work was financed by Chilean Nucleus NC120066. GS and NA acknowledge support by FONDECYT grants
1120040 and # 1150913, MR by Fondecyt grant # 1131055, and FL by Fondecyt grant # 1151427.

References

Adams, J. M., Faure, H., Faure-Denard, L., McGlade, J. M., and Woodward, F. I. (1990). Increase in terrestrial carbon storage from the Last Glacial Maximum to the present. *Nature*, 348:711–714.

Adkins, J. F., McIntyre, K., and Schrag, D. P. (2002). The Salinity, Temperature, and δ^{18}O of the Glacial Deep Ocean. *Science*, 298:1769–1773.

Adkins, J. F. and Schrag, D. P. (2002). Reconstructing Last Glacial Maximum bottom water salinities from deep-sea sediment pore fluid profiles. *Earth and Planetary Science Letters*, 16:109–123.

Anderson, R. F., Ali, S., Bradtmiller, L., Nielsen, S. H. H., Fleisher, M. Q., Anderson, B. E., and Buckle, L. H. (2009). Wind-Driven Upwelling in the Southern Ocean and the Deglacial Rise in Atmospheric CO_2. *Science*, 323:1443–1448.

Bonan, G. B. (2008). Forests and Climate Change: Forcings, Feedbacks, and the Climate Benefits of Forests. *Science*, 320:1444.

Bouttes, N., Paillard, D., and Roche, D. M. (2010). Impact of brine-induced stratification on the glacial carbon cycle. *Climate of the Past*, 6:681–710.

Bouttes, N., Paillard, D., Roche, D. M., Brovkin, V., and Bopp, L. (2011). Last Glacial Maximum CO_2 and δ^{13}C successfully reconciled. *Geophysical Research Letters*, 38:L02705.

Broecker, W. and Barker, S. (2007). A 190‰ drop in atmosphere's Δ^{14}C during the "Mystery Interval" (17.5 to 14.5 kyr). *Earth and Planetary Science Letters*, 256:90–99.

Brovkin, V., Ganopolski, A., Archer, D., and Rahmstorf, S. (2007). Lowering of glacial atmospheric CO_2 in response to changes in oceanic circulation and marine biogeochemistry. *Paleoceanography*, 22:PA4202.

Brovkin, V., Hofmann, M., Bengtsen, J., and Ganopolski, A. (2002). Ocean biology could control atmospheric δ^{13}C during glacial-interglacial cycle. *Geochemistry Geophysics Geosystems*, 3(5).

Burke, A. and Robinson, L. F. (2012). The Southern Ocean's Role in Carbon Exchange During the Last Deglaciation. *Science*, 335:557–561.

Chapin, I. I. I., Stuart, F., Matson, P. A., and Vitousek, P. (2011). *Principles of terrestrial ecosystem ecology*.

Ciais, P., Tagliabue, A., Cuntz, A., Bopp, L., Scholze, M., Hoffmann, G., Lourantou, A., Harrison, S. P., Prentice, I. C., Kelley, D. I., Koven, C., and Piao, S. L. (2012). Large inert carbon pool in the terrestrial biosphere during the Last Glacial Maximum. *Nature Geoscience*, 5:74–79.

Crichton, K. A., Bouttes, N., Roche, D. M., Chappellaz, J., and Krinner, G. (2016). Permafrost carbon as a missing link to explain CO_2 changes during the last deglaciation. *Nature*, 9:683–687.

Curry, W. B. and Oppo, D. W. (2005). Glacial water mass geometry and the distribution of δ^{13}C of $\sum CO_2$ in the western Atlantic Ocean. *Paleoceanography*, 20:PA1017.

Davidson, E. A. and Janssens, I. A. (2006). Temperature sensitivity of soil carbon decomposition and feedbacks to climate change. *Nature*, 440(7081):165–173.

d'Orgeville, M., Sijp, W. P., England, M. H., and Meissner, K. J. (2010). On the control of glacial-interglacial atmospheric CO_2 variations by the Southern Hemisphere westerlies. *Geophysical Research Letters*, 37:L21703.

Fischer, H., Schmitt, J., Lüthi, D., Stocker, T. F., Tschumi, T., Parekh, P., Joos, F., Köhler, P., Völker, C., Gersonde, R., Barbante, C., Le Floch, M., Raynaud, D., and Wolff, E. (2010). The role of Southern Ocean processes on orbital and millennial CO_2 variations - a synthesis. *Quaternary Science Reviews*, 29 (1):193–205.

Francois, R., Altabet, M. A., Yu, E.-F., Sigman, D. M., Bacon, M. P., Frank, M., Bohrmann, G., Bareille, G., and Labeyrie, L. D. (1997). Contribution of Southern Ocean surface-water stratification to low atmospheric CO_2 concentrations during the last glacial period. *Nature*, 389:929–935.

Friedlingstein, P., Cox, P., Betts, R., Bopp, L., von Bloh, W., Brovkin, V., Cadule, P., Doney, S., Eby, M., Fung, I., Bala, G., John, J., Jones, C., Joos, F., Kato, T., Kawamiya, M., Knorr, W., Lindsay, K., Matthews, H. D., Raddatz, T., Rayner, P., Reick, C., Roeckner, E., Schnitzler, K.-G., Schnur, R., Strassmann, K., Weaver, A. J., Yoshikawa, C., and Zeng, N. (2006). Climate-carbon cycle feedback analysis: Results from the C^{4}MIP model Intercomparison. *Journal of Climate*, 19:3337–3353.

Gerber, S., Joos, F., and Prentice, C. (2004). Sensitivity of a dynamic global vegetation model to climate and atmospheric CO_2. *Global Change Biology*, 10:1223–1239.

Gower, S. T., Kucharik, C. J., and Norman, J. M. (1999). Direct and indirect estimation of leaf area index, f$_A PAR$, and net primary production of terrestrial ecosystems. *Remote sensing of environment*, 70(1):29–51.

Hain, M. P., Sigman, D. M., and Haug, G. H. (2014). Distinct roles of the Southern Ocean and North Atlantic in the deglacial atmospheric radiocarbon decline. *Earth and Planetary Science Letters*, 394:198–208.

Hartmann, D. L. (1994). Global Physical Climatology. *Elsevier*, New York:357pp.

Huiskamp, W. N. and Meissner, K. J. (2012). Oceanic carbon and water masses during the Mystery Interval: A model-data comparison study. *Paleoceanography*, 27:PA4206.

Jaccard, S. L., Galbraith, E. D., Fröhlicher, T. L., and Gruber, N. (2014). Ocean (de)oxygenation across the last deglaciation: Insights for the future. *Oceanography*, 27 (1):26–35.

Khvorostyanov, D. V., Ciais, P., Krinner, G., and Zimov, S. A. (2008). Vulnerability of east Siberia's frozen carbon stores to future warming. *Geophysical Research Letters*, 35:L10703.

Kohfeld, K. E. and Ridgwell, A. (2009). Glacial-Interglacial Variability in Atmospheric CO_2. *Geophysical Research Series*, 187:251–286.

Köhler, P., Knorr, G., and Bard, E. (2014). Permafrost thawing as a possible source of abrupt carbon release at the onset of the Bølling/Allerød. *Nature Communications*, 5:5520.

Kwon, E. Y., Hain, M. P., Sigman, D. M., Galbraith, E. D., Sarmiento, J. L., and Toggweiler, J. R. (2012). North Atlantic ventilation of "southern-sourced" deep water in the glacial ocean. *Paleoceanography*, 27:PA2208.

Laj, C., Kissel, C., and Beer, J. (2004). High resolution global paleointensity stack since 75 kyr (GLOPIS-75) calibrated to absolute values. *in: Geophysical Monograph Series (AGU)*, 145:255–265.

Lambeck, K., Rouby, H., Purcell, A., Sun, Y., and M., S. (2014). Sea level and global ice volumes from the Last Glacial Maximum to the Holocene. *PNAS*, 111 (43):15296–15303.

Lambert, F., Kug, J.-S., Park, R. J., Mahowald, N., Winckler, G., Abe-Ouchi, A., O'ishi, R., Takemura, T., and Lee, J.-H. (2013). The role of mineral-dust aerosols in polar temperature amplification. *Nature Climate Change*, 3:487–491.

Lambert, F., Tagliabue, A., Shaffer, G., Lamy, F., Winckler, G., Farias, L., Gallardo, L., and De Pol-Holz, R. (2015). Dust fluxes and iron fertilization in Holocene and Last Glacial Maximum climates. *Geophysical Research Letters*, 42(14):6014–6023.

Lamy, F., Gersonde, R., Winckler, G., Esper, O., Jaeschke, A., Kuhn, G., Ullermann, J., Martinez-Garcia, A., Lambert, F., and Kilian, R. (2014). Increased Dust Deposition in the Pacific Southern Ocean During Glacial Periods. *Science*, 343:403–407.

Lüthi, D., Le Floch, M., Bereiter, B., Blunier, T., Barnola, J. M., Siegenthaler, U., Raynaud, D., Jouzel, J., Fischer, H., Kawamura, K., and Stocker, T. F. (2008). High-resolution carbon dioxide concentration record 650,000-800,000 years before present. *Nature*, 453:379–382.

Maher, B. A., Prospero, J. M., Mackie, D., Gaiero, D., Hesse, P., and Balkanski, Y. (2010). Global connections between aeolian dust, climate and ocean biogeochemistry at the present day and at the last glacial maximum. *Earth-Science Reviews*, 99:61–97.

Mahowald, N., Kohfeld, K. E., Hansson, M., Balkanski, Y., Harrison, S. P., Prentice, I. C., Schulz, M., and Rodhe, H. (1999). Dust sources and deposition during the last glacial maximum and current climate: A comparison of model results with paleodata from ice cores and marine sediments. *Journal of Geophysical Research*, 104 (D13):15895–15916.

Mahowald, N., Yoshioka, M., Collins, W., Conley, A., Fillmore, D., and Coleman, D. (2006a). Climate response and radiative forcing from mineral aerosols during the glacial maximum, pre-industrial, current and doubled-carbon dioxide climates. *Geophysical Research Letters*, 33:L20705.

Mahowald, N. M., Muhs, D. R., Levis, S., Rasch, P. J., Yoshioka, M., Zender, C. S., and Luo, C. (2006b). Change in atmospheric mineral aerosols in response to climate: Last glacial period, preindustrial, modern, and doubled carbon dioxide climates. *Journal of Geophysical Research*, 111:D10202.

Mariotti, V., Paillard, D., Bopp, L., Roche, D. M., and Bouttes, N. (2016). A coupled model for carbon and radiocarbon evolution during the last deglaciation. *Radiocarbon*, Geophysical Research Letters(43):1306–1313.

Mariotti, V., Paillard, D., Roche, D. M., Bouttes, N., and Bopp, L. (2013). Simulated Last Glacial Maximum $\Delta^{14}C_{atm}$ and the deep glacial ocean carbon reservoir. *Radiocarbon*, 55(2-3):1595–1602.

Martin, J. H., Gordon, R. M., and Fitzwater, S. E. (1990). Iron in Antarctic waters. *Nature*, 345:156–158.

Martínez-García, A. M., Sigman, D. M., Ren, H., Anderson, R. F., Straub, M., Hodell, D. A., Jaccard, S. L., Eglinton, T. I., and Haug, G. H. (2014). Iron Fertilization of the Subantarctic Ocean During the Last Ice Age. *Science*, 343(6177):1347–1350.

Matney, M. (2012). On the Probability of Random Debris Reentry Occuring on Land or Water. *Orbital Debris Quaterly News*, 16(1):5.

Monnin, E., Indermühle, A., Daellenbach, A., Flueckiger, J., Stauffer, B., Stocker, T. F., Raynaud, D., and Barnola, J.-M. (2001). Atmospheric CO_2 concentrations over the Last Glacial Termination. *Science*, 291:112–114.

Muscheler, R., Beer, J., Wagner, G., Laj, C., Kissel, C., Raisbeck, G. M., Yiou, F., and Kubik, P. W. (2004). Changes in the carbon cycle during the last deglaciation as indicated by the comparison of ^{10}Be and ^{14}C records. *Earth and Planetary Science Letters*, 219:325–340.

Okazaki, Y., Timmermann, A., Menviel, L., Harada, N., Abe-Ouchi, A., Chikamoto, M. O., Mouchet, A., and Asahi, H. (2010). Deepwater Formation in the North Pacific During the Last Glacial Termination. *Science*, 329:200–204.

Peltier, W. R. (2004). Global Glacial Isostasy and the Surface of the Ice-Age Earth: The ICE-5G (VM2) Model and GRACE. *Annual Review of Earth and Planetary Sciences*, 32:111–149.

Peng, C. H., Guiot, J., and van Campo, E. (1998). Estimating changes in terrestrial vegetation and carbon storage: Using paleoecological data and models. *Quaternary Science Reviews*, 17:719–735.

Prentice, K. C. and Fung, I. Y. (1990). The sensitivity of terrestrial carbon storage to climate change. *Nature*, 346:48–51.

Prentice, K. C., Harrison, S. P., and Bartlein, P. J. (2011). Global vegetation and terrestrial carbon cycle changes after the last ice age. *Nature*, 189:988–998.

Reimer, P. J., Baillie, M. G. L., Bard, E., Bayliss, A., Beck, J. W., Blackwell, P. G., Bronk Ramsey, C., Buck, C. E., Burr, G. S., Edwards, R. L., Friedrich, M., Grootes, P. M., Guilderson, T. P., Hajdas, I., Heaton, T. J., Hogg, A. G., Hughen, K. A., Kaiser, K. F., Kromer, B., McCormac, F. G., Manning, S. W., Reimer, R. W., Richards, D. A., Southon, J. R., Talamo, S., Turney, C. S. M., van der Plicht, J., and Weyhenmeyer, C. E. (2009). INTCAL09 and MARINE09 radiocarbon age calibration curves, 0-50,000 years cal BP. *Radiocarbon*, 51, Nr. 4:1111–1150.

Reimer, P. J., Bard, E., Bayliss, A., Beck, J. W., Blackwell, P. G., Ramsey, C. B., Buck, C. E., Cheng, H., Edwards, R. L., Friedrich, M., Grootes, P. M., Guilderson, T. P., Haflidason, H., Hajdas, I., Hatté, C., Heaton, T. J., Hoffmann, D. L., Hogg, A. G., Hughen, K. A., Kaiser, K. F., Kromer, B., Manning, S. W., Niu, M., Reimer, R. W., Richards, D. A., Scott, E. M., Southon, J. R., Staff, R. A., Turney, C. S. M., and van der Plicht, J. (2013). INTCAL13 and MARINE13 radiocarbon age calibration curves 0–50,000 years cal BP. *Radiocarbon*, 55, Nr. 4:1869–1887.

Rose, K. A., Sikes, E. L., Guilderson, T. P., Shane, P., Hill, T. M., Zahn, R., and Spero, H. J. (2010). Upper-ocean-to-atmosphere radiocarbon offsets imply fast deglacial carbon dioxide release. *Nature*, 466(7310):1092–1097.

Saugier, B., Roy, J., and Mooney, H. A. (2001). 23 - Estimations of global terrestrial productivity: converging toward a single number. *Terrestrial global productivity: past, present and future*, pages 543–557.

Schaefer, K., Zhang, T., Bruhwiler, T., and Barrett, A. P. (2011). Amount and timing of permafrost carbon release in response to climate warming. *Tellus*, 63B:165–180.

Schmitt, J., Schneider, R., Elsig, J., Leuenberger, D., Lourantou, A., Chappellaz, J., Köhler, Joos, F., Stocker, T. F., Leuenberger, M., and Fischer, H. (2012). Carbon Isotope Constraints on the Deglacial CO_2 Rise from Ice Cores. *Science*, 336:710–714.

Schuur, E. A. G., Bockheim, J., Canadell, J. G., Euskirchen, E., Field, C. B., Goryachkin, S. V., Hagemann, S., Kuhry, P., Lafleur, P. M., Lee, H., Mazhitova, G., Nelson, F. E., Rinke, A., Romanovsky, V. E., Shiklomanov, N., Tarnocai, C., Venevsky, S., Vogel, J. G., and Zimov, S. A. (2008). Vulnerability of Permafrost Carbon to Climate Change: Implications for the Global Carbon Cycle. *Bioscience*, 58:701–714.

Schuur, E. A. G., McGuire, A. D., Schädel, C., Grosse, G., Harden, J. W., Hayes, D. J., Hugelius, G., Koven, C. D., Kuhry, P., Lawrence, D. M., Lawrence, D. M., Natali, S. M., Olefeldt, D., Romanovsky, V. E., Schaefer, K., Turetsky, M. R., Treat, C. C., and Vonk, J. E. (2015). Climate change and the permafrost carbon feedback. *Nature*, 520(7546):171–179.

Shaffer, G. (1996). Biogeochemical cycling in the global ocean: 2. New production, Redfield ratios, and remineralization in the organic pump. *Journal of Geophysical Research*, 101:3723–3745.

Shaffer, G. (2010). Long-term effectiveness and consequences of carbon dioxide sequestration. *Nature Geoscience*, 3:464–467.

Shaffer, G., Malskær Olsen, S., and Pepke Pedersen, J. (2008). Presentation, calibration and validation of the low-order, DCESS Earth System Model (Version 1). *Geoscientific Model Development*, 1:17–51.

Shaffer, G., Olsen, S. M., and Pedersen, O. P. (2009). Long-term ocean oxygen depletion in response to carbon dioxide emissions from fossil fuels. *Nature Geoscience*, 2:105–109.

Shaffer, G. and Sarmiento, J. L. (1995). Biogeochemical cycling in the global ocean: 1. A new analytical model with continuous vertical resolution and high latitude dynamics. *Journal of Geophysical Research*, 100:2659–2672.

Shakun, J., Clark, P. U., He, F., Marcott, S. A., Mix, A. C., Liu, Z. Y., Otto-Bliesner, B., Schmittner, A., and Bard, E. (2012). Global warming preceded by increasing carbon dioxide concentrations during the last deglaciation. *Nature*, 484:49–54.

Sigman, D. M. and Boyle, E. A. (2000). Glacial/interglacial variations in atmospheric carbon dioxide. *Nature*, 407:859–869.

Sigman, D. M., Hain, M. P., and Haug, G. H. (2010). The polar ocean and glacial cycles in atmospheric CO_2 concentration. *Nature*, 466:47–55.

Sterner, R. W. and Elser, J. J. (2002). *Ecological Stoichiometry: The Biology of Elements from Molecules to the Biosphere*, volume 25(9). Princeton University Press.

Toggweiler, J. R. and Russel, J. (2008). Ocean circulation in a warming climate. *Nature*, 451(17):286–288.

Waelbroeck, C., Labeyrie, L., Michel, E., Duplessy, J. C., McManus, J. F., Lambeck, K., Balbon, E., and Labracherie, M. (2002). Sea-level and deep water temperature changes derived from benthic foraminifera isotopic records. *Quaternary Science Reviews*, 21:295–305.

Watson, A. J. and Naveira Garabato, A. C. (2006). The role of Southern Ocean mixing and upwelling in glacial-interglacial atmospheric CO$_2$ change. *Tellus*, 58B:73–87.

Zech, R. (2012). A permafrost glacial hypothesis - Permafrost carbon might help explaining the Pleistocene ice ages. *Quaternary Science Journal*, 61(1):84–92.

Zheng, D., Prince, S., and Wright, R. (2003). Terrestrial net primary production estimates for 0.5 grid cells from field observations - a contribution to global biogeochemical modeling. *Global Change Biology*, 9(1):46–64.

Zickfeld, K., Eby, M., Weaver, A. J., Alexander, K., Crespin, E., Edwards, N. R., Eliseev, A. V., Feulner, G., Fichefet, T., Forest, C. E., Friedlingstein, P., Goosse, H., Holden, P. B., Joos, F., Kawamiya, M., Kicklighter, D., Kienert, H., Matsumoto, K., Mokhov, I. I., Monier, E., Olsen, S. M., Pedersen, J. O. P., Perrette, M., Philippon-Berthier, G., Ridgwell, A., Schlosser, A., Schneider Von Deimling, T., Shaffer, G., Sokolov, A., Spahni, R., Steinacher, M., Tachiiri, K., Tokos, K. S., Yoshimori, M., Zeng, N., and Zhao, F. (2013). Long-term climate change commitment and reversibility: An EMIC intercomparison. *Journal of Climate*, 26(16):5782–5809.